Mathematisch-Naturwissenschaftliche Fakultät
Ernst-Moritz-Arndt-Universität Greifswald

Bachelor Thesis

Particle model of the Magnus effect

Philipp Kanehl
Greifswald, 12.07.2010

Gutachter:
Prof. Dr. Ralf Schneider
PD Dr. Alexander Quandt

Table of Contents

Table of Contents . . . iii

1 Introduction . . . 1

2 Basics . . . 3
2.1 Aerodynamic characteristics of rotating objects . . . 3
2.2 Rarefied gas flow . . . 5

3 Numerical and analytical methods . . . 7
3.1 Analytical model . . . 7
3.1.1 Solid cylinder . . . 8
3.1.2 Rectangular bodies . . . 9
3.1.3 Regular n-sided polygon . . . 10
3.2 Numerical approach . . . 12

4 Results . . . 13
4.1 Simulation results of particles interacting with a cylinder . . . 13
4.1.1 Velocity variation . . . 13
4.1.2 α variation . . . 14
4.1.3 Variation of radius . . . 14
4.1.4 Variation of density . . . 15
4.1.5 Error analysis . . . 15
4.2 Simulation results of particles interacting with a rotating rectangular body . . . 17
4.2.1 Rectangular 1:1 . . . 17
4.2.2 Rectangular 1:2 . . . 18
4.2.3 Rectangular 1:100 . . . 21
4.3 Regular n-sided polygon . . . 22
4.3.1 Triangle . . . 23
4.3.2 Hexagon . . . 24

5 Conclusion and outlook . . . 27

Bibliography . . . 29

Acknowledgements . . . 31

Chapter 1

Introduction

The interaction of a rotating body with a flowing medium is of greatest interest in aerospace, but also in sports. In 1997 Roberto Carlos prepares to carry out his free kick in a soccer game between Brazil and France. He stands 32 meters distant from the goal blocked by a human wall of four players of the French team, so that no direct shot would find the goal. Carlos knows that a successful shot is still possible using a special technique. Executing the shot he applies in addition to the translational velocity a side spin to the ball changing the aerodynamic properties so that next to drag and gravity force another force gets important. This force alters the trajectory of the ball from a simple parabolic to a characteristically curved one, making its way round the wall and for the keeper very difficult to predict. This effect is called the "Magnus effect" and the force "Magnus force", respectively. The German physicist Heinrich Magnus was the first who introduced a correct mathematical description for this effect in 1852. However, Isaac Newton was the first to record the effect and to give an explanation. In 1672 he published his work "*A new theory about light and colors*" where he tried to explain optical refraction, the bending of a ray of light when it passes through a prism. He used the analogon to a curved trajectory of a spinning tennis ball. [1]: "For, a circular as well as a progressive motion..., it parts on that side, where the motions conspire, must press and beat the contiguous air more violently than on the other, and there excite a reluctancy and reaction of the air proportionably greater."

For small angular velocities the Magnus force acting on a ball even changes its direction. This effect is referred to as "inverse Magnus effect". A swirling ball in soccer or volleyball combines alternating Magnus and inverse Magnus force by changing its velocity regime. During its trajectory the ratio of angular to translational velocity is modified and the different Magnus forces are initiated. The inverse Magnus effect also occurs in rarefied gases which will be the main subject of this work. A rarefied gas or fluid is characterized through a relatively large mean free path of the fluid particles. In comparison to the mean free path, dimensions of boundaries confining the stream are relatively small. The ratio of free mean path and characteristic dimension is given by the Knudsen number, which is large for a rarefied gas. As a result particle to boundary or particle to projectile impacts are much more frequent than particle to particle impacts, ensuring that deflected particles do not influence the incoming stream.

Rarefied gas flow dynamics and inverse Magnus effects are used in contamination investigations. For instance in a hard disk drive (HDD) [2] the gap between the slider and the disc is about ten times smaller than the mean free path of air, which is around 65nm. This gives a Knudsen number much greater than one. In this rarefied gas regime inverse Magnus forces on rotating spherical shaped particles occur. Knowing the acting forces contaminations can be predicted and HDDs optimized.

The article published by Patrick D. Weidman and Andrzej Hercynski [3] provides an analytical model to calculate drag and Magnus forces on different rotating geometries in rarefied gases. The aim of this thesis is to develop and validate a numerical approach for calculating the interaction of rotating bodies in free molecular flow. In both models collisions between particles in the flow are neglected consistent with the regime of rarefied flow.

In chapter 2 the aerodynamic characteristics of rotating objects and the regime of rarefied gas flow will be discussed. In chapter 3 the analytical and numerical models will be introduced. In

chapter 4 the results are presented for different geometries such as cylinder, rectangle, triangle and hexagon. Drag and lift forces will be computed including an error propagation analysis. Finally, in chapter 5 the thesis will be summarized.

Chapter 2

Basics

2.1 Aerodynamic characteristics of rotating objects

On ballistic spinning objects in flight, forces and moments are acting uniquely determining the trajectory. These forces and moments include the gravitational force, aerodynamic force, and an aerodynamic moment which acts to slow down the spinning motion. Unforeseen wind gusts and other changes in atmospheric conditions makes a calculation of the trajectory difficult. In research, experiments are conducted in a controlled environment (wind tunnels) to minimize the effect of atmospheric anomalies. For numerical computations, simplified conditions are assumed.
The aerodynamic force is the total of drag and lift force. The lift force is also called the Magnus force named after his discoverer the German physicist Heinrich Magnus. He described the effect of force acting perpendicular to the line of motion of a spinning ball in 1852.

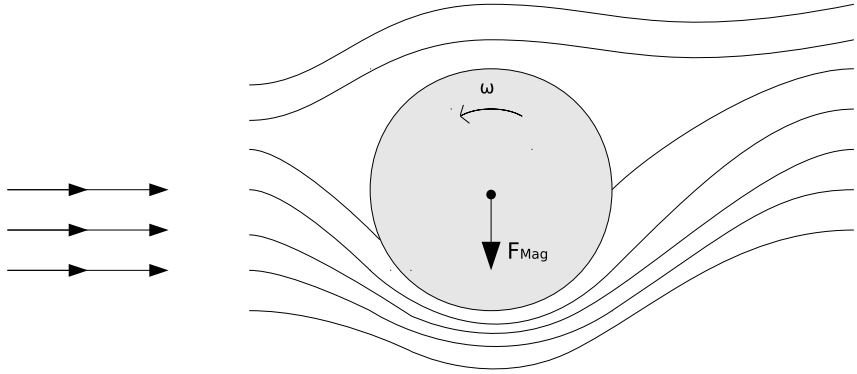

Figure 2.1: The Magnus effect, demonstrated on a ball. Lines represent the wind velocity, and the arrow F_{Mag} represents the resulting force towards the side of lower pressure.

The explanation of the Magnus Effect is a relatively simple one [4]. When any object is moving through a fluid, such as air, its surface interacts with a thin layer of air known as the boundary layer. In the case of the sphere or ball, the boundary layer separates from the surface, creating a wake or low-pressure region behind ball. The front-to-back pressure difference creates a backward force on the ball, which slows the forward motion of the ball. This is the normal air resistance, or aerodynamic drag, that acts on every object. However, if the ball is spinning as it moves, the boundary layer separates at different points on opposite sides of the ball, further upstream on the side of the ball that is turning into the airflow, and further downstream on the side turning with the airflow. Consequently, the air flowing around the ball is deflected slightly sideways, resulting in an asymmetrical wake behind the ball as shown in Fig. (2.1). If it is assumed that the air in the wake has upwards or positive momentum, for momentum to be conserved the ball must possess an equal but opposite or downwards momentum. Hence a sideways deflection in the trajectory occurs. The magnitude and direction of this resulting momentum vector and its corresponding Magnus force is directly dependent on the velocity

vector $\mathbf{v}$, angular velocity vector ω, Magnus coefficient C_{M}, cross- sectional ball area A and air density ρ.

$$F_{\mathrm{Mag}} = \frac{1}{2}\rho A v^2 C_{\mathrm{M}} \frac{\omega \times \mathbf{v}}{|\omega \times \mathbf{v}|} \tag{2.1}$$

The drag force is a retarding force characterized in terms of the drag coefficient C_{d}.

$$F_{\mathrm{drag}} = -\frac{1}{2}\rho A v^2 C_{\mathrm{d}} \frac{\mathbf{v}}{|\mathbf{v}|} \tag{2.2}$$

The dimensionless Magnus coefficients C_{M} and C_{d} scale the strength of drag force or Magnus force at a particular speed v and spin ratio $\omega R/v$. C is also a function of the Reynolds number Re and the roughness ratio κ of the surface. The Reynolds number expresses the ratio of inertial (resistant to change or motion) forces to viscous (heavy and gluey) forces and is defined as:

$$Re = \frac{vL}{\nu} \tag{2.3}$$

Where L can be a characteristic dimension of the body itself like the diameter of the ball, but also the scale of a boundary the flow is confined to, like the diameter of a wind tunnel probe. The coefficient ν is the kinematic viscosity of the flow.
Another relevant ratio for the aerodynamics is the Knudsen number Kn. This as well dimensionless number is defined as the ratio of the molecular mean free path λ to the characteristic length L.

$$Kn = \frac{\lambda}{L} \tag{2.4}$$

The Knudsen number is related to the more familiar parameters of fluid mechanics, the Mach number M and the Reynolds number Re. From kinetic theory it is known that

$$\nu = \frac{1}{2}\lambda \overline{v}. \tag{2.5}$$

Where $\overline{v}$ is the mean molecular speed and ν is the kinematic viscosity. The mean speed is related to the speed of sound c as follows:

$$c = \overline{v}\sqrt{\frac{\pi\gamma}{8}} \tag{2.6}$$

Here γ is the isentropic exponent. The combination of Eq. (2.5) and (2.6) as well as the substitution of $Re = vL/\nu$ and $Kn = \lambda/L$ yields the fundamental relation

$$Kn = 1.26\sqrt{\gamma}\frac{M}{Re}. \tag{2.7}$$

2.2 Rarefied gas flow

Rarefied gas flow models have been subject to many investigations lately, confined to the case of very slow speeds. In a rarefied gas flow the length of the molecular mean free path λ is comparable to some characteristic dimension L of the flow field and therefore the Knudsen number Kn is not negligibly small, so that the gas does not behave entirely as a continuous fluid. The regime termed as "free molecular flow" starts at conditions [5]:

$$\frac{M}{Re} > 3 \tag{2.8}$$

It classifies a regime of extreme rarefaction. The body is located in the rarefied flow of infinite extent. Particles reemitted after striking the surface of the body travel very far before colliding with other particles. It is therefore valid to neglect the effect of reemitted particles on the incoming stream. These basic assumptions lead to the fact that neither boundary layer nor shock waves like for a continuous flow are formed in the vicinity of the object. A typical example is the re-entry of vehicle or satellites into the upper atmosphere [6].
The Magnus force sometimes changes direction in this regime. This change is attributable to the decreasing role of shear stresses and increase in the contribution of normal stresses [7]. This "inverse Magnus effect", as it will be referred to prospectively, in particular takes place at huge Knudsen numbers.

$$Kn >> 1$$

Under this condition simple particle models can be applied. Newton's model [8] of fluid resistance "consists of equal particles freely disposed at equal distances from each other", impacting the body surface such that their tangential momentum is preserved while the normal momentum is transferred to the body. While this model is useful at hypersonic speeds, it is not applicable to a subsonic flow. The particle model used in this work differs from Newton's assumptions in following terms:

- The particle mass m is orders of magnitudes smaller than the rotating objects mass.
- Impacts with the object are perfectly elastic.
- The fraction of tangential momentum acquired by the particle from the rotation of the body is measured in α, the Maxwellian accommodation coefficient [9].

Chapter 3

Numerical and analytical methods

3.1 Analytical model

The analytical calculations presented here follow Patrick D.Weidman and Andrzej Herczynski [3]. Free particles are assumed in a homogeneous density flow, which impacts the body at a velocity v. The body spins with an angular velocity ω. In 2-dimensional Cartesian coordinates the flow direction is considered to be parallel to the x axis $\mathbf{e_x}$ in positive direction while the body is rotating about a fixed axis of symmetry at $\mathbf{r_{rot}} = (0, 0)$. The number of particles impacting a surface element area dS of the body per unit time is $N = n_0 v|\mathbf{e_x} \cdot \mathbf{n}|dS$. n_0 describes the density of the flow and $\mathbf{n}$ is the unit normal to the body surface.
The pre-impact momentum of a specific particle is $\mathbf{p} = (mv, 0)$ and $\mathbf{p}' = (p'_x, p'_y)$ after repulsion. As a result, the momentum acting on the body is

$$\Delta\mathbf{p} = (p_x - p'_x, p_y - p'_y). \tag{3.1}$$

The force on a surface element is then $\mathbf{f} = N \cdot \Delta\mathbf{p}$. Integration over the surface exposed to the molecular flow gives the total acting force on the body.

$$\mathbf{F} = n_0 v \int_{\text{upwind}} \Delta\mathbf{p} \cdot |\mathbf{e_x} \cdot \mathbf{n}| dS \tag{3.2}$$

Impacts with the body are considered to be perfectly elastic and its mass orders of magnitudes larger than the particle mass.
To generate an inverse Magnus force acting on the body it is essential that a fraction of tangential momentum is acquired by the particle. This fraction will be measured in α.

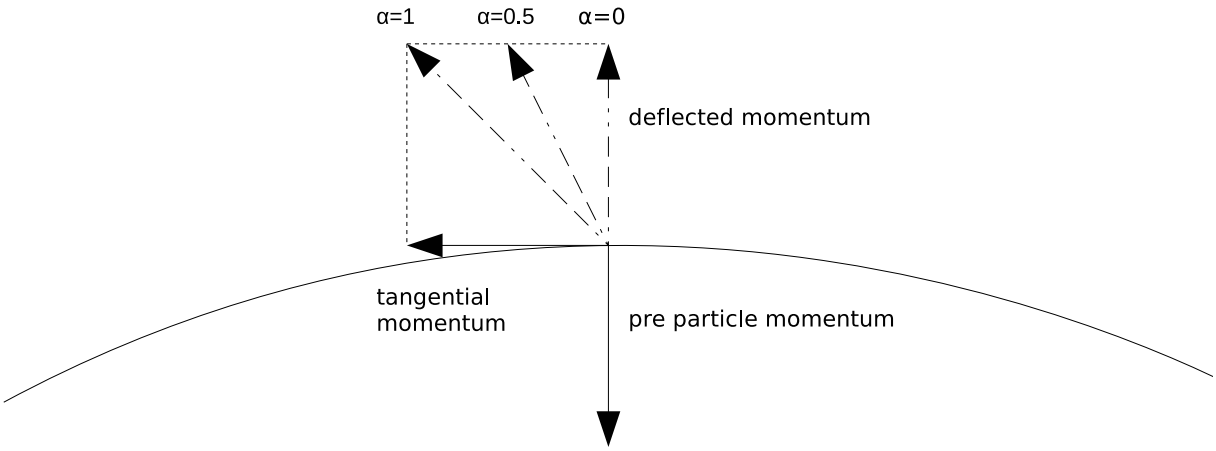

Figure 3.1: Tangential momentum acquired by particle.

3.1.1 Solid cylinder

The simplest test case of a two-dimensional system is a cylinder. Cylindrical coordinates (r, φ) shown in Fig. (3.2) are used. Then, the surface fraction is $dS = Rd\varphi$ and $\mathbf{e_x} \cdot \mathbf{n} = \sin\varphi$.

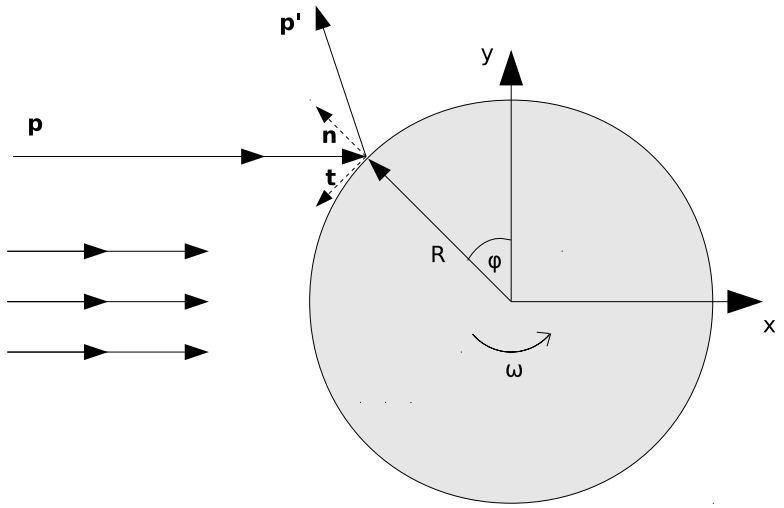

Figure 3.2: Cylindrical body rotating about an axes of symmetry at origin.

In order to calculate the deflected momentum of a particle interacting with the rotating cylinder the velocity vector before the impact has to be calculated with respect to the tangential momentum of the cylinder.

$$\mathbf{v} \rightarrow \mathbf{v} - \alpha\omega R \cdot \begin{pmatrix} \cos\varphi \\ \sin\varphi \end{pmatrix}$$

After impact the normal component gets reversed while the tangential component preserves.

$$\mathbf{v}' = -(\mathbf{v} \cdot \mathbf{n})\mathbf{n} + (\mathbf{v} \cdot \mathbf{t})\mathbf{t}$$

With $\mathbf{t} = (-\cos\varphi, -\sin\varphi)$, $\mathbf{n} = (-\sin\varphi, \cos\varphi)$ and Eq. (3.1) the momentum changes are:

$$\Delta p_x = mv(1 - \cos 2\varphi) + m\alpha\omega R\cos\varphi \quad (3.3)$$

$$\Delta p_y = m\alpha\omega R\sin\varphi - mv\sin 2\varphi \quad (3.4)$$

Integration of Eq. (3.2) yields the acting drag and lift forces:

$$F_x = mn_0 Rv\int_0^\pi d\varphi(v(1-\cos 2\varphi) + \alpha\omega R\cos\varphi)\sin\varphi = \frac{8}{3}mn_0 Rv^2 \quad (3.5)$$

$$F_y = mn_0 Rv\int_0^\pi d\varphi(\alpha\omega R\sin\varphi - v\sin 2\varphi)\sin\varphi = \frac{\pi}{2}mn_0\alpha R^2\omega v \quad (3.6)$$

With $M = mn_0\pi R^2$ the total mass of the particles displaced by the cylinder, a steady-state

inverse Magnus force of the body is obtained which is proportional to $M/2$.

$$F_{\mathrm{Mag}} = \frac{M}{2}\omega v$$

3.1.2 Rectangular bodies

The calculation of the Magnus force for bodies of non-circular section is more complex. A rectangular-like body (see Fig. (3.3)) with $a \times b$ dimension undergoing a uniform rotation ω at the centroid of the section. $\xi = \omega t$ is measured clockwise from the y-axis determining the current angle of the body. Indices 1 and 2 indicate if the upper or lower side is considered. The coordinates r_1 and φ locate points on the upper face with borders $\varphi_- = -\arctan(a/b)$ and $\varphi_+ = \arctan(a/b)$.

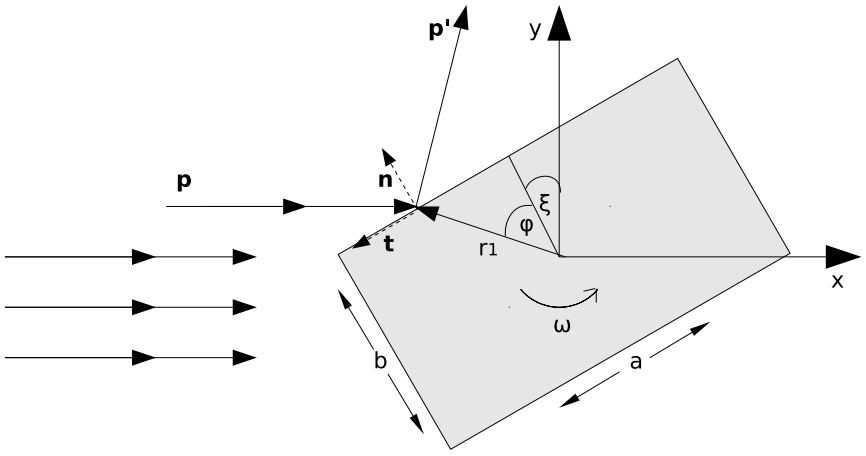

Figure 3.3: Particles impacting a spinning rectangular body.

Considering that only the angular momentum tangential to the surface is transferred to a particle the velocity vector right before the impact is:

$$\mathbf{v} \to \mathbf{v} - \alpha\omega r_1 \cos\varphi \cdot \begin{pmatrix}\cos\xi \\ \sin\xi\end{pmatrix}$$

with $r_1 = \frac{b}{2\cos\varphi}$. Like for the cylinder, the normal component gets reversed while the tangential component preserves.

$$\mathbf{v}' = -(\mathbf{v}\cdot\mathbf{n})\mathbf{n} + (\mathbf{v}\cdot\mathbf{t})\mathbf{t}$$

With $\mathbf{t} = (-\cos\xi, -\sin\xi)$, $\mathbf{n} = (-\sin\xi, \cos\xi)$ and Eq. (3.1) the momentum changes are:

$$\Delta p_x = mv(1-\cos 2\xi) - m\alpha\omega\frac{b}{2}\cos(\xi) \tag{3.7}$$

$$\Delta p_y = -mv\sin 2\xi + m\alpha\omega\frac{b}{2}\sin(\xi) \tag{3.8}$$

The number of collisions per unit time impacting an area element dy_1 is $N = n_0 v dy_1$. With $y_1 = r_1\cos(\xi+\varphi)$ it can be rewritten as:

$$N = -n_0 v\frac{b}{2}\frac{\sin\xi}{\cos^2\varphi}d\varphi \tag{3.9}$$

Integration of Eq. (3.2) over the upper side finally yields:

$$F_{x,1} = \frac{mn_0vb}{2}\sin\xi \int_{\varphi_+}^{\varphi_-} d\varphi \left[v\frac{(\cos 2\xi - 1)}{\cos^2\varphi} - \alpha\omega b\frac{\cos(\xi)}{2\cos^3\varphi}\right] = mn_0v\left(2av\sin^3\xi + \frac{ab}{2}\alpha\omega\sin\xi\cos\xi\right) \tag{3.10}$$

$$F_{y,1} = \frac{mn_0vb}{2}\sin\xi \int_{\varphi_+}^{\varphi_-} d\varphi \left[\frac{v\sin 2\xi}{\cos^2\varphi} - \alpha\omega b\frac{sin(\xi)}{2\cos^3\varphi}\right] = mn_0v\left(\frac{ab}{2}\alpha\omega\sin^2\xi - av\sin 2\xi\sin\xi\right) \tag{3.11}$$

A similar analysis for the lower face (2) gives $F_{x,2}$ and $F_{y,2}$ and after summation of both contributions one obtains the total force:

$$F_{\text{drag}} = 2mn_0v^2(a\sin^3\xi + b\cos^3\xi) \tag{3.12}$$

$$F_{\text{lift}} = mn_0v^2(b\cos\xi - a\sin\xi)\sin 2\xi + \frac{1}{2}M\alpha\omega v \tag{3.13}$$

Here $M = mn_0ab$ is again the mass of gas displaced by the rectangular body. It is worth noting that there is no dependency on the current body angle ξ for the Magnus force $1/2M\alpha\omega v$.

3.1.3 Regular n-sided polygon

Finally, we take the general case of a right parallelepiped rotating about the centroid of it's regular polygon section, displayed in Fig. (3.4). Only the Magnus force will be calculated, hence the drag force will be not discussed. The number of faces exposed to the particle stream depends on whether n is odd or even. If n is even we have usually $n/2$ sides in the flow and for a short time only just $n/2-1$. If n is odd, depending on the angle either $\frac{n+1}{2}$ or $\frac{n-1}{2}$ are exposed.

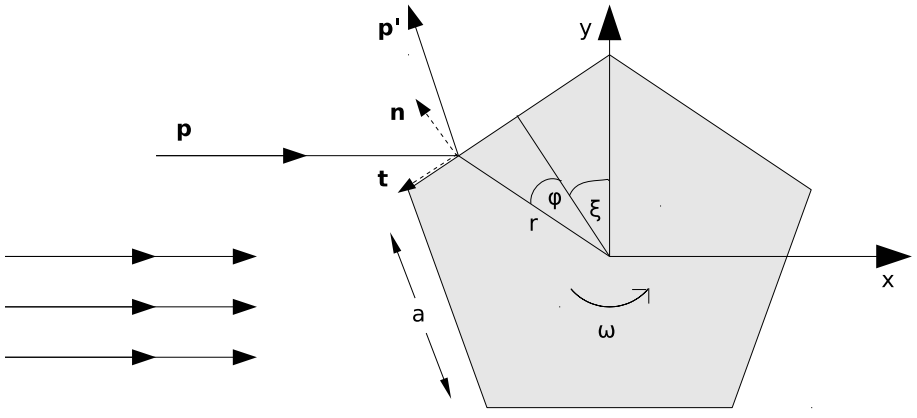

Figure 3.4: Particles impacting a spinning regular pentagon.

Like for the rectangular case each exposed side is marked with an index i. In principle the integration is the same like for the rectangular body, however additionally an angle offset δ_i is introduced to access all faces.

$$\delta_i = (i-1)\frac{2\pi}{n} \tag{3.14}$$

The radius r for a n-sided polygon is:

$$r = \frac{a}{2}\cot\left(\frac{\pi}{2}\right)\frac{1}{\cos\varphi} \tag{3.15}$$

The integration is the same as in Eq. (3.11). Taking into account that $b = a$ and accounting also for the additional factor $\cot(\pi/n)$ from the radius, the Magnus force for the ith face can be calculated:

$$(F_i)_{\mathrm{Mag}} = mn_0\alpha\omega v\frac{a^2}{2}\cot\left(\frac{\pi}{n}\right)\sin^2(\xi+\delta_i) \tag{3.16}$$

Summation over the total number I of exposed sides gives the total Magnus force for the parallelepiped:

$$F_{\mathrm{Mag}} = mn_0\alpha\omega v\frac{a^2}{2}\cot\left(\frac{\pi}{n}\right)\sum_{i=1}^{I}\sin^2(\xi+\delta_i) \tag{3.17}$$

Using explicit forms [10] one gets:

Case 1: n even
Here the sum yields $n/4$, so we get a steady-state inverse Magnus force:

$$F_{\mathrm{Mag}} = mn_0\alpha\omega v\frac{a^2}{8}n\cot\left(\frac{\pi}{n}\right) = \frac{M}{2}\alpha\omega v \tag{3.18}$$

with the mass of gas displaced by the body $M = mn_0a^2n\cot(\pi/4)/4$.

Case 2: n odd
Here, one has to distinguish if the maximum or the minimum number of faces is exposed.

Maximum number of exposed faces:

$$F_{\mathrm{Mag}} = mn_0\alpha\omega v\frac{a^2}{8}n\cot\left(\frac{\pi}{n}\right)\left[n + 2\sin^2\xi - \tan\left(\frac{\pi}{n}\right)\sin 2\xi\right] \tag{3.19}$$

Minimum number of exposed faces:

$$F_{\mathrm{Mag}} = mn_0\alpha\omega v\frac{a^2}{8}n\cot\left(\frac{\pi}{n}\right)\left[n - \frac{\sin 3\xi}{\sin\xi} + 2\frac{\sin\left(\frac{3\pi}{n}\right)}{\sin\left(\frac{2\pi}{n}\right)}\cos\left(2\xi - \frac{\pi}{n}\right)\right] \tag{3.20}$$

It is worth noticeable that a regular n-sided polygon for the limit case $n \to \infty$ leads back to the formula of a cylinder by diminishing side length a using $a_n\cot(\pi/n)/2 = R$ and Eq. (3.19).

$$F_{\mathrm{Mag}} = mn_0\alpha\omega v\frac{R^2}{2}n\tan\left(\frac{\pi}{n}\right)$$

Since $\lim_{n\to\infty}[n\tan(\pi/n)] = \pi$ we yield the expected Eq. (3.6).

3.2 Numerical approach

The numerical approach calculates for individual particles the momentum transferred to the body for each particle hitting the body surface. Momenta and locations of the body and every particle are known for every time step, therefore it's easily possible to investigate the acting forces in dependence of the spinning body's angle. Time steps are discretized to Δt, therefore during a single time step a particle moves the distance $\Delta t\mathbf{v}$ and a point $\mathbf{b}$ on the body surface experiences a rotation which is described by following rotation matrix:

$$\mathbf{b}' = \begin{pmatrix} \cos\omega\Delta t & \sin\omega\Delta t \\ -\sin\omega\Delta t & \cos\omega\Delta t \end{pmatrix}\mathbf{b}$$

If no impact from a particle i is detected its position $\mathbf{r}_{i,t}$ is reset to $\mathbf{r}_{i,t+\Delta t}$ after traveling a straight distance $\Delta t\mathbf{v}$. In case its trajectory intersects a body surface element, the location of the intersection is calculated. The normal component of momentum gets reversed while the tangential component preserves, just like in the analytical model, and a new velocity is computed. The particle $\mathbf{r}_{i,t+\Delta t}$ gets replaced at the appropriate location based on the location of the intersection (see Fig. (3.5)).

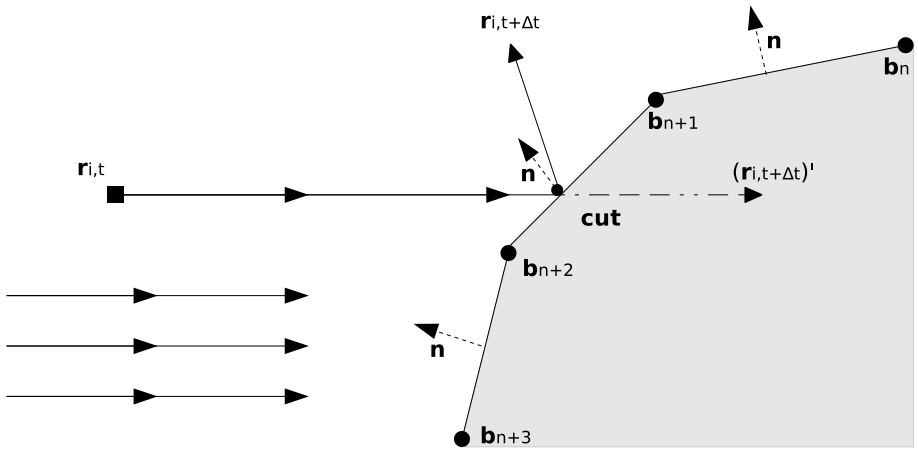

Figure 3.5: Particle intersecting the surface of a body.

The particles spawn randomly right in front of the rotating body with same velocity $\mathbf{v}$. Due to the fact that a free molecular flow is modeled the particles are not interacting with each other but only with the body surface. This qualifies the model to accomplish the inverse Magnus effects in rarefied gas flows, which will be discussed in the following chapter.

Chapter 4

Results

4.1 Simulation results of particles interacting with a cylinder

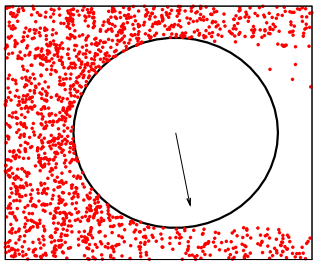

The first geometry to investigate is a rotating cylinder. The cross section of the cylinder is represented numerically by 100 small surface elements arranged to a circle. The rotation angle of the cylinder has no influence on the acting forces hence the impacting momenta are summed up over a long time and afterwards divided by this averaging time to get the mean force.

4.1.1 Velocity variation

Firstly, the dependence on the particle velocity is studied. The analytical solutions have shown that one can expect a square velocity dependency for the drag (Eq. (3.5)) due to the particle flow vector $n_0 \mathbf{v} dS$ (number of particles striking surface element dS per time) combined with the momentum vector $m\mathbf{v}$ itself. The Magnus force compensates the momentum fractions in y-direction from upper and lower side so that it exhibits a linear dependency (Eq. (3.6)).

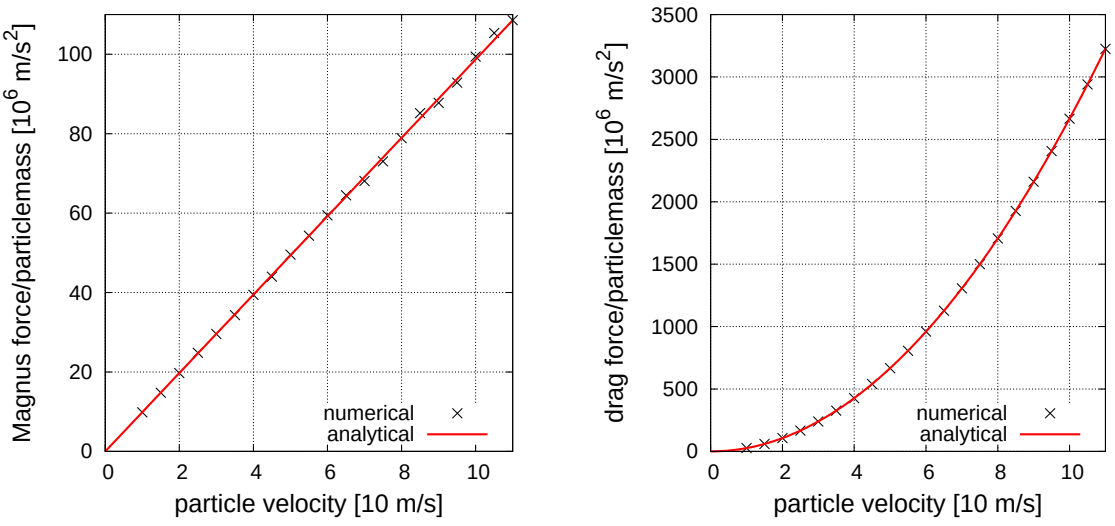

Figure 4.1: Left: acting Magnus force as a function of particle velocity, right: acting drag force as a function of particle velocity, $R = 0.1\text{m}$, $\alpha = 1$, $\omega = 20\pi\text{s}^{-1}$, $n_0 = 10^6\text{m}^{-2}$.

4.1.2 α variation

Here, the dependency of the Magnus force on α is studied. A linear scaling for the Magnus force with α and a constant drag force is expected.

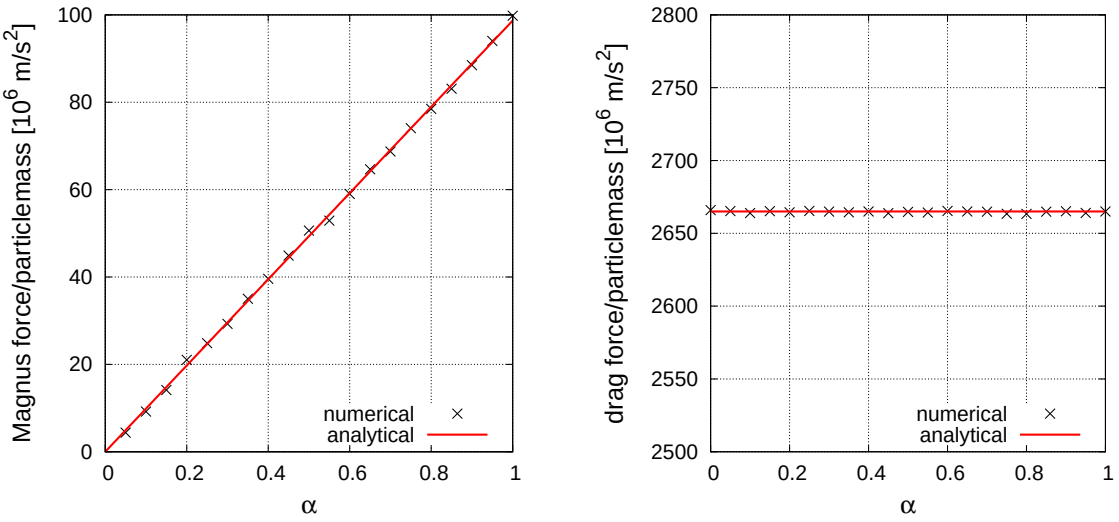

Figure 4.2: Left: acting Magnus force as a function of the accommodation coefficient, right: acting drag force as a function of the accommodation coefficient, $R = 0.1\text{m}$, $v = 100\text{ms}^{-1}$, $\omega = 20\pi\text{s}^{-1}$, $n_0 = 10^6\text{m}^{-2}$.

As expected, α has no influence on the drag force. The tangential momentum fractions in x-direction transferred from the body to particles at the upper and lower side of the cylinder cancel each other. For each particle a momentum is assigned proportional to α, so one gets a linear scaling of the Magnus force.

4.1.3 Variation of radius

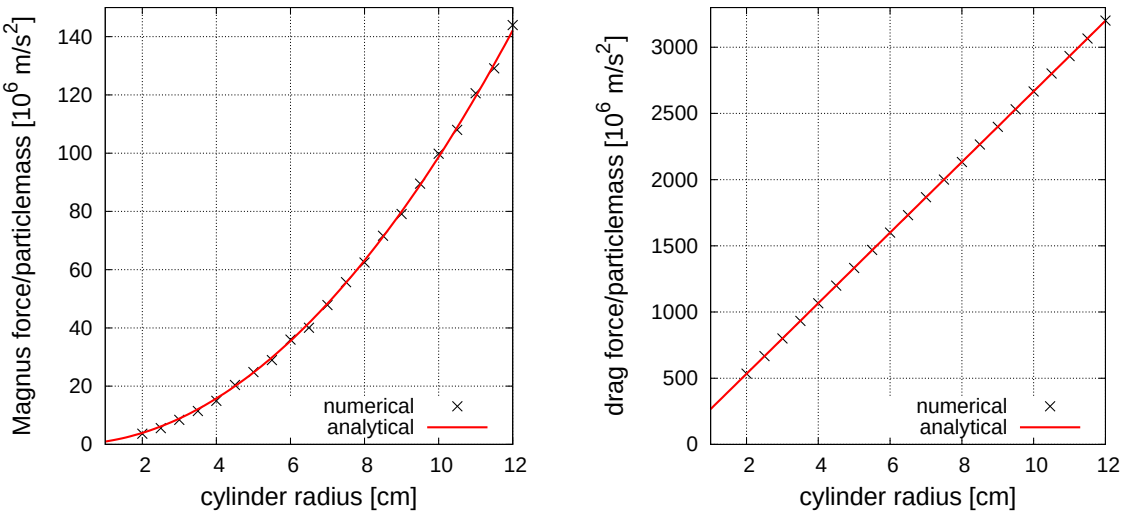

Figure 4.3: Left: acting Magnus force as a function of the radius, right: acting drag force as a function of the radius, $\alpha = 1$, $v = 100\text{ms}^{-1}$, $\omega = 20\pi\text{s}^{-1}$, $n_0 = 10^6\text{m}^{-2}$.

With a variation of the radius R a square dependence of the Magnus force on the radius is obtained as a result of the integration over the upwind side which yields a factor R which is multiplied with each particle's tangential momentum $mR\omega$. After integration the latter has no contribution to the drag force resulting in a R proportionality.

4.1.4 Variation of density

The last quantity to vary is the particle density. It has no direct influence on the momentum calculations but changes the number of particles hitting the surface. During the time Δt the cylinder gets struck by $n_0 v \Delta t 2R$ particles which grows linear with n_0. Therefore a linear scaling of drag and Magnus force is obtained for $\alpha > 0$.

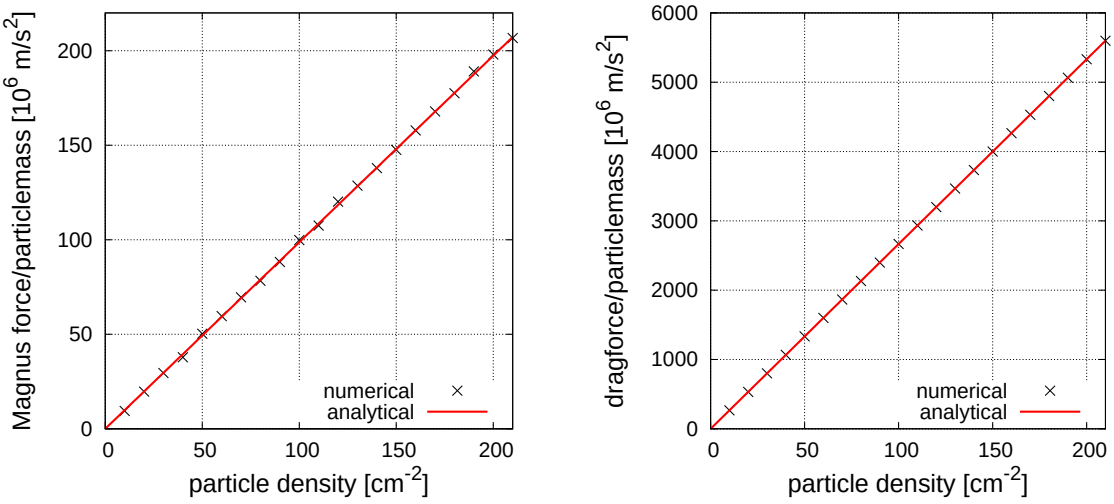

Figure 4.4: Left: acting Magnus force as a function of particle density, right: acting drag force as a function of particle density, $\alpha = 1$, $v = 100\mathrm{ms}^{-1}$, $\omega = 20\pi\mathrm{s}^{-1}$, $R = 0.1\mathrm{m}$.

4.1.5 Error analysis

Apparently, the analytical and numerical solutions of all quantities agree within statistical variations. Numerical values for the Magnus force are not as smooth as for the drag force. This is a result of the fact that the Magnus force has the same standard deviation like the drag force, but at the same time is orders of magnitude smaller. This will be analysed in the following.
From Eqs. (3.3) and (3.4) it becomes clear that both Magnus and drag force have a mv contribution from the momentum of the particle, and a $m\omega R$ contribution from the applied momentum of the rotating body. After upwind side integration for the drag force the assigned angular momentum and for Magnus force the particle momentum disappears. If now the density is subject to fluctuations, errors for both have to be analysed. To calculate this error the particle flow is divided into equal lanes, each lane leading to another surface fraction of the cylinder so that the whole body is covered. Ideally, each lane should contain the same amount of particles N/l whereas N is the total number of particles and l the number of lanes. But due to the random sampling of the particles inhomogeneities occur. The particles of a single lane can be approximated with a *Poisson*-distribution (for high N and l).
Hence the error for one lane can be estimated:

$$\Delta n_i = \pm\sqrt{\frac{N}{l}}$$

The error for the force depends on the lane where fluctuations occur. The overall error is obtained after summation of each lane.

$$\frac{\Delta f_{\mathrm{Mag,i}}}{m} = \Delta n_i(v(1-\cos 2\varphi_i) + \alpha\omega R\cos\varphi_i) \Rightarrow \Delta F_{\mathrm{Mag}} = \sum_{i=1}^{l} \Delta f_{\mathrm{Mag,i}}$$

$$\frac{\Delta f_{\mathrm{drag,i}}}{m} = \Delta n_i(\alpha\omega R\sin\varphi_i - v\sin 2\varphi_i) \Rightarrow \Delta F_{\mathrm{drag}} = \sum_{i=1}^{l} \Delta f_{\mathrm{drag,i}}$$

Because N is constant

$$\sum_{i=1}^{l} \Delta n_i = 0$$

holds. Δn_i is either $+\sqrt{N/l}$ or $-\sqrt{N/l}$ so one gets $l/2$ from each. For 20 lanes this combines

$$\frac{20!}{10!10!} = 184756$$

opportunities for arrangement of distinguishable lanes.
For case of the cylinder the number of particles impacting the body per millisecond from one lane is $2Rvn_0/20 = 1000\mathrm{s}^{-1}$. The fluctuation per millisecond is therefore $\Delta n_i = \pm\sqrt{1000} = \pm 31,62$. Calculating the errors for all 184756 opportunities and assorting the results at occurrence gives the *Gaussian*-distribution displayed in Fig. (4.5).

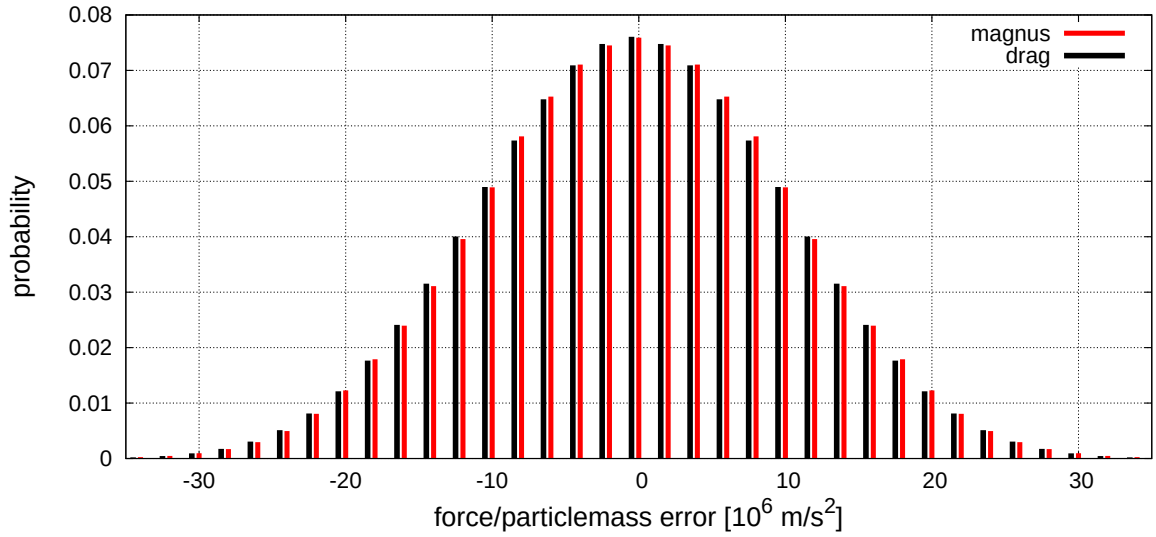

Figure 4.5: Error distribution *Gaussian* function: $\alpha = 1$, $v = 100\mathrm{ms}^{-1}$, $\omega = 20\pi\mathrm{s}^{-1}$, $R = 0.1\mathrm{m}$, $n_0 = 10^6\mathrm{m}^{-2}$.

Surprisingly, drag and Magnus error cover the same *Gaussian*-function which leads to the same standard deviation of both $\sigma \approx 8 \cdot 10^6 \frac{\mathrm{m}}{\mathrm{s}^2} m_{\mathrm{particle}}$ but to different relative errors Δ_{rel}:

$$\Delta_{\mathrm{rel,Mag}} = \frac{2\sigma}{\frac{\pi}{2}mn_0\alpha R^2\omega v} \approx 16,2\% \qquad \Delta_{\mathrm{rel,drag}} = \frac{2\sigma}{\frac{8}{3}mn_0 Rv^2} \approx 0,6\%$$

Taking into account that the results in section 4.1 are the average over 20 milliseconds one gets additionally the factor $\frac{1}{\sqrt{20}} \approx 0,22$.

4.2 Simulation results of particles interacting with a rotating rectangular body

In this section the interaction with a rotating rectangular body is calculated. To model a rectangle just 4 surface elements were necessary so that adequate computing times could be achieved even for a high particle density. Compared to the case of the cylinder phase-resolved investigations will be done due to different lift and drag forces at different angles. Therefore, the mean value can not be taken over a longer time interval but just for the discretized time Δt. Consequently, much less particles impacts contribute leading to large statistical variations. To counteract this effect the particle density got increased by ten.

4.2.1 Rectangular 1:1

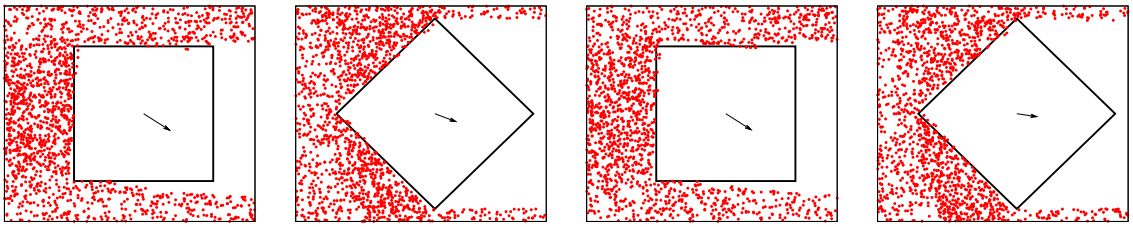

The first object to analyse is a square. For the forces in dependency of the body angle, a π periodical function for every rectangle and in case of the square even a $\pi/2$ periodicity is expected. For $\alpha = 1$ compared with $\alpha = 0$ a constant offset of $\frac{M}{2}\alpha\omega v$ is anticipated with the mass of particles displaced by the body $M = mn_0ab$.
The simulations for the case of the rotating square gave the following results:

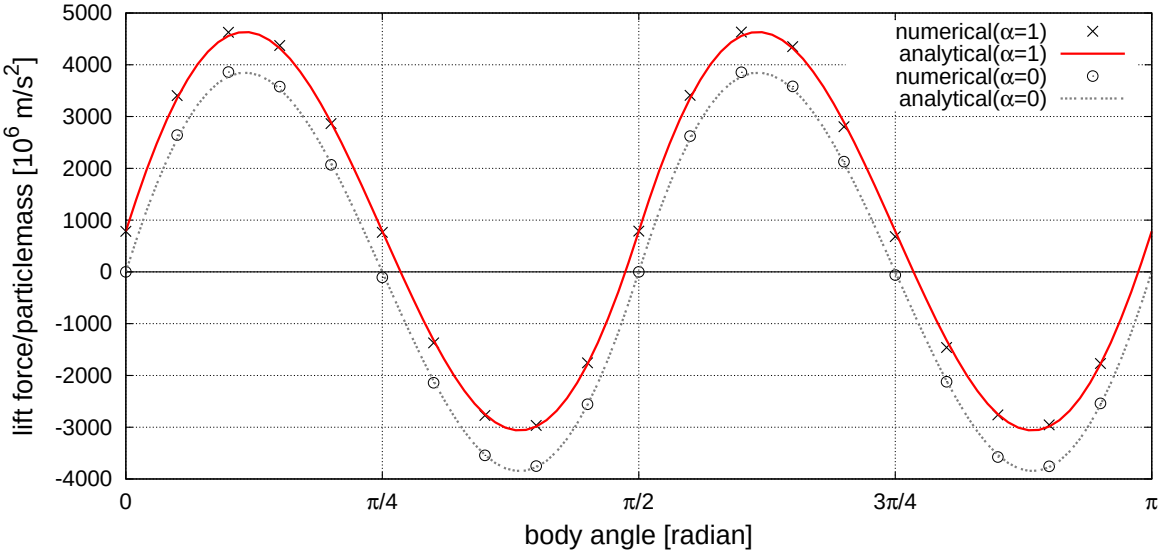

Figure 4.6: Lift force for a square as a function of rotation angle, $a = b = 0.1\text{m}$, $v = 100\text{ms}^{-1}$, $\omega = 5\pi/100\text{s}^{-1}$, $n_0 = 10^7\text{m}^{-2}$.

Numerical solutions agree very well with the analytical results. The lift force reaches its peaks with a $\frac{\pi}{8}(2n+1)$ periodicity when one side stands on a plain $\pi/8$ angle on the flow where it is

no counterbalance to the almost orthogonal side, due to less counted impacts. Its zero-points get reached either when both sides equally share the flow (lift forces from both sides cancel down each other) or one side stands exactly orthogonal on the flow ($\frac{\pi}{8} \cdot 2n$ periodicity). The lift force for $\alpha = 1$ is respectively higher than for $\alpha = 0$ due to the offset of the Magnus force.
Analytically, the constant Magnus force can be extracted from Eq. (3.13):

$$\begin{aligned} \frac{F_{\text{Mag,analytic}}}{m} &= \frac{1}{2} m n_0 a b \alpha \omega v \\ &= 250\pi \cdot 10^6 \frac{\text{m}}{\text{s}^2} \approx 785.4 \cdot 10^6 \frac{\text{m}}{\text{s}^2} \end{aligned}$$

Numerically (see Fig. (4.6)), the double standard deviation of the mean is:

$$\frac{F_{\text{Mag,numeric}}}{m} = (763.91 \pm 31.18) 10^6 \frac{\text{m}}{\text{s}^2}$$

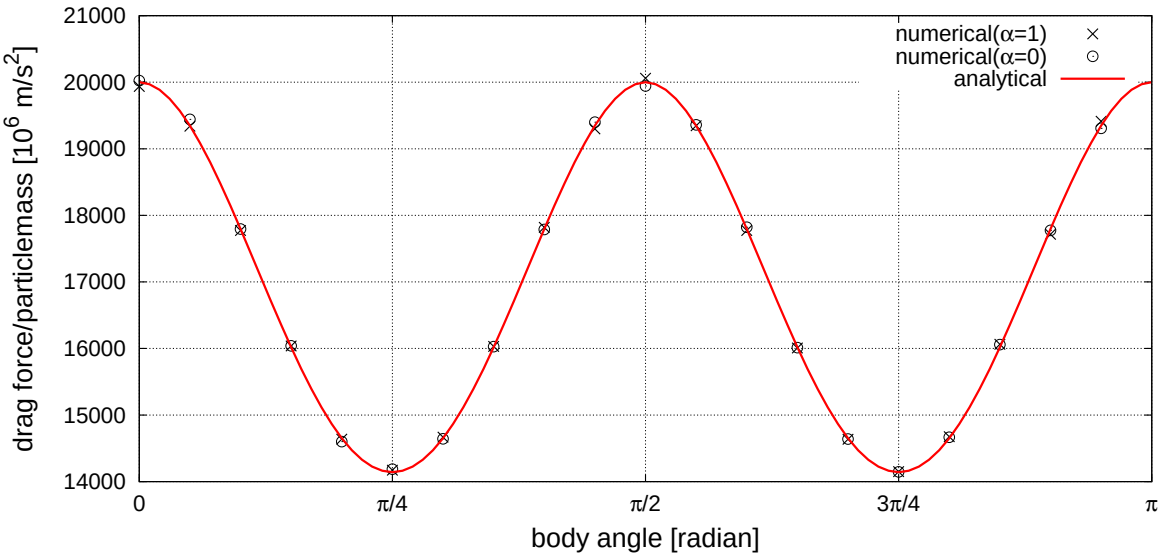

Figure 4.7: Drag force for a square as a function of rotation angle, $a = b = 0.1\text{m}$, $v = 100\text{ms}^{-1}$, $\omega = 5\pi/100\text{s}^{-1}$, $n_0 = 10^7\text{m}^{-2}$.

For the drag force in Fig. (4.7) no change is expected according to the analytical results from variations of α. This is not a general case for every arbitrary spinning geometry but a rather special situation for cylinder and rectangular bodies.
One can verify that the drag force has its peaks always when one side stands orthogonal on the flow, because particles get redirected in the opposite direction. Its minima get reached when all particles get redirected in y-direction (both sides on 45 degree angle on the flow). In conclusion one can say that for $\alpha = 0$ drag force always reaches extrema when lift force intersects the zero axis.

4.2.2 Rectangular 1:2

After scaling down side b to a half, the $\pi/4$ periodicity is no longer preserved. This has neither consequences for a constant Magnus force nor for the independence of the drag force of α. Apart from reducing $b = 10\text{cm}$ to $b = 5\text{cm}$ the simulation got started with the same quantities

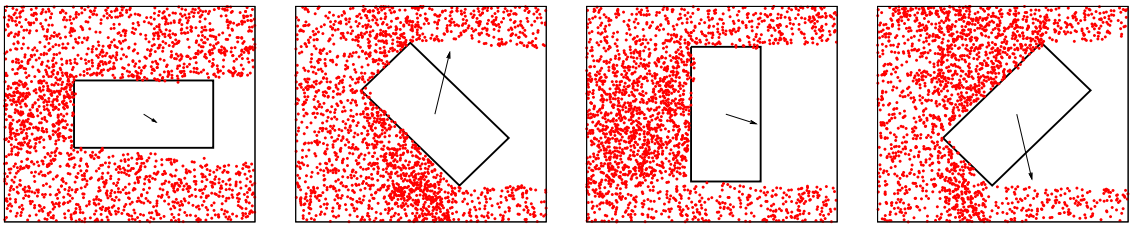

like for the square, therefore half of the Magnus force as for the square (10×10) can be expected because just half of the particle mass get displaced from the rectangular (10×5).
The simulations for the rotating rectangular body has provided following results:

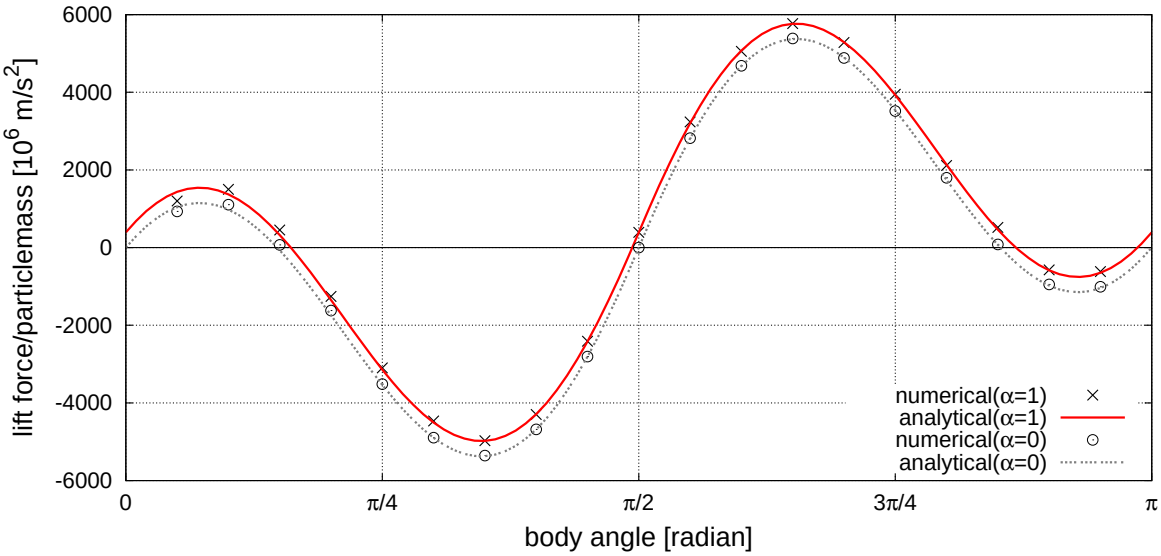

Figure 4.8: Lift force for a rectangle as a function of rotation angle, $a = 0.1\text{m}$, $b = 0.05\text{m}$, $v = 100\text{ms}^{-1}$, $\omega = 5\pi/100\text{s}^{-1}$, $n_0 = 10^7\text{m}^{-2}$.

Analytically, the constant Magnus force is:

$$\frac{F_{\text{Mag,analytic}}}{m} = 125\pi \cdot 10^6 \frac{\text{m}}{\text{s}^2} \approx 392.70 \cdot 10^6 \frac{\text{m}}{\text{s}^2}$$

Numerically, using Fig. (4.8), the double standard deviation of the mean is:

$$\frac{F_{\text{Mag,numeric}}}{m} = (386.99 \pm 17.30)10^6 \frac{\text{m}}{\text{s}^2}$$

A more detailed examination of the Magnus force contribution will follow in chapter 4.3 for the example of the triangle as well as the hexagon. The shifting of the peaks and some zero-points is noticeable in Fig. (4.8) compared to Fig. (4.6). Looking at $\alpha = 0$, fixed zero points are achieved if the body lies evenly in the flow. This happens for side b at angle 0 and for a at $\pi/2$. The other two can be calculated by setting Eq. (3.13) equal to zero which results in

$$\frac{b}{a} = \tan\varphi_0 \longrightarrow \frac{1}{2} = \tan\varphi_0 \Longleftrightarrow \varphi_{01} \approx 0.59 \cdot \frac{\pi}{4}$$

for the b to a rotation and

$$\frac{a}{b} = \tan(\varphi_0 - \pi/2) \longrightarrow 2 = \tan(\varphi_0 - \pi/2) \Longleftrightarrow \varphi_{02} \approx 3.41 \cdot \frac{\pi}{4}$$

for the a to b rotation. Respectively, the angles where the lift force from side a is identical with the lift force from the b side. The differentiation of Eq. (3.13) $0 = \frac{dF_{\text{lift}}}{d\varphi}$ yields

$$\frac{\tan 2\varphi_m}{2} = \frac{b(a)\cos\varphi_m - a(b)\sin\varphi_m}{b(a)\sin\varphi_m + a(b)\cos\varphi_m}$$

,
which is untransposable. Graphical solution provides for the peaks:

$$\varphi_{\text{max1}} \approx 0.288 \cdot \frac{\pi}{4} \qquad \varphi_{\text{max2}} \approx 2.614 \cdot \frac{\pi}{4}$$

and for the minima:

$$\varphi_{\text{min1}} \approx 1.386 \cdot \frac{\pi}{4} \qquad \varphi_{\text{min2}} \approx 3.713 \cdot \frac{\pi}{4}$$

The drag force is as predicted independent of α. Like for the square it has its peaks when one side is exposed to the flow. Logically, the half sized b side produces half the drag force than the a side. Looking at Eq. (3.12) it appears that the drag force has its bottoms exactly when the ($\alpha = 0$) lift force reaches a zero point. Differentiation of this equation gives:

$$\frac{dF_{\text{lift}}}{d\varphi} = \text{const} \cdot (3a(b)\cos\varphi\sin^2\varphi - 3b(a)\sin\varphi\cos^2\varphi) = 0$$

$$\longrightarrow \tan\varphi_m = \frac{b(a)}{a(b)} \tag{4.1}$$

which is indeed the same equation as for the lift force zero intersection. Hence, we can generalize the concluding statement for any arbitrarily rectangular figure. Drag force reaches extrema always when lift force intersects the zero axis. This also means that if the drag force reaches a minimum the total acting force of the body is the lowest.

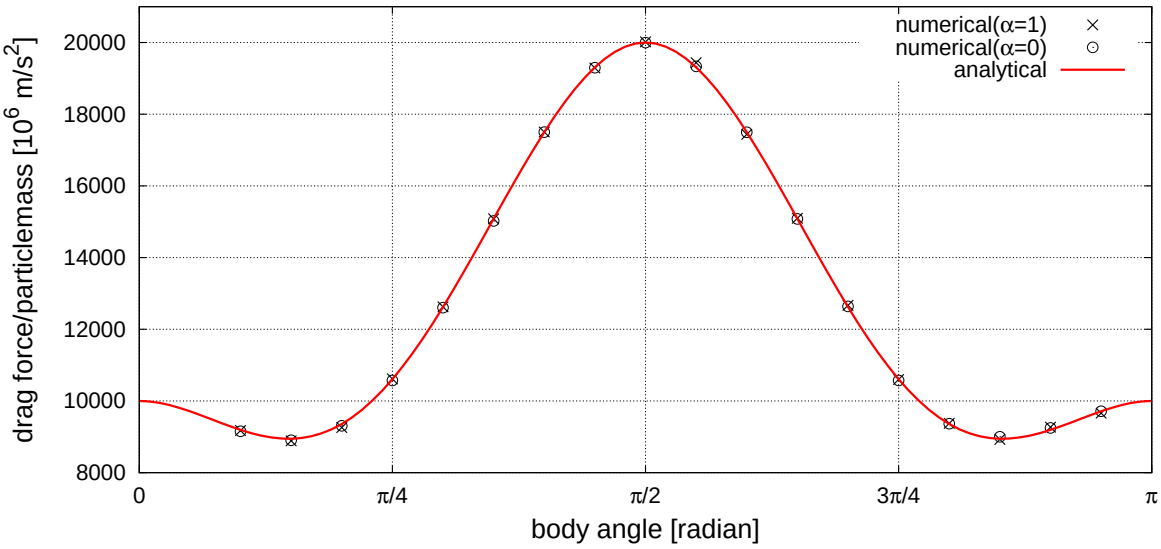

Figure 4.9: Drag force for a rectangle as a function of rotation angle, $a = 0.1\text{m}$, $b = 0.05\text{m}$, $v = 100\text{ms}^{-1}$, $\omega = 5\pi/100\text{s}^{-1}$, $n_0 = 10^7\text{m}^{-2}$.

4.2.3 Rectangular 1:100

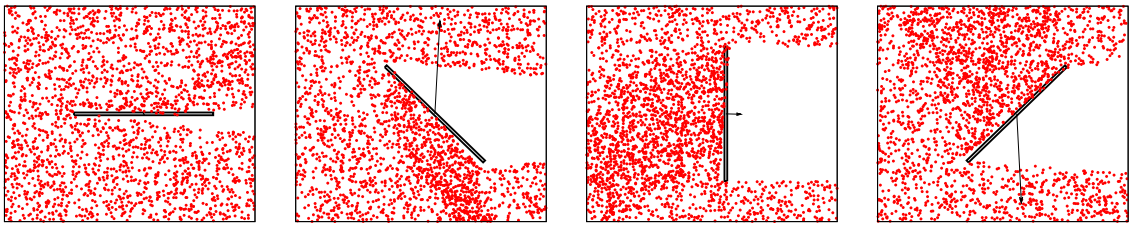

The last rectangular case to investigate is an approximation of a flat plate. Numerically, this is accomplished by scaling b down to a hundredth of a. Whereas the analytical solution Eqs. (3.12) and (3.13) can be simplified with $b \to 0$ to:

$$\mathbf{F} = 2mn_0av^2 \sin^2\varphi(\sin\varphi\mathbf{e_x} - \cos\varphi\mathbf{e_y}) \tag{4.2}$$

Looking at Fig. (4.10) no offset is seen for $\alpha = 1$, because every tangential unit vector is orthogonal to the velocity vector at every point of the spinning plate.

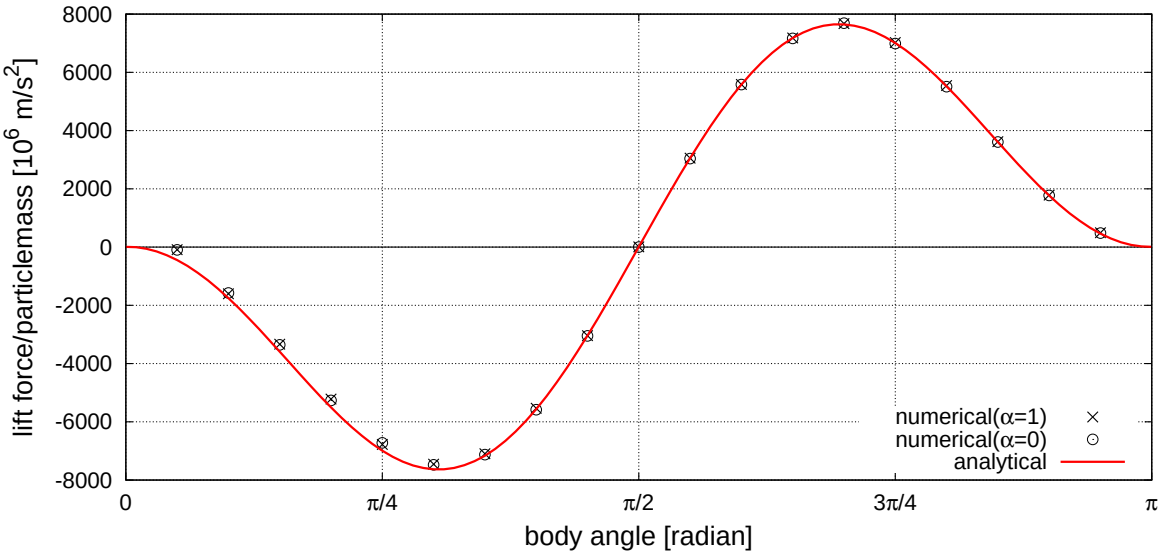

Figure 4.10: Lift force of a flat plate as a function of rotation angle, $a = 0.1\text{m}$, $b = 0.001\text{m}$, $v = 100\text{ms}^{-1}$, $\omega = 5\pi/100\text{s}^{-1}$, $n_0 = 10^7\text{m}^{-2}$.

Evaluating zero points and extreme values is quite easy. The zero intersections in between the orthogonal orientations to the flow ($n\frac{\pi}{2}$ $n = 0, 1, 2..$), cf. Fig. (4.6) and (4.8), have disappeared due to the fact that side b is to small to act as a counterbalance to a.
The peak for the lift force does not get reached at a 45 degree angle to the flow as naively expected because impacts at this angle change the momentum direction in a 90 degree angle. The peak appears at slightly larger angle as seen in Fig. (4.10). Differentiation of the lift force fraction of Eq. (4.2) provides the condition for this peak:

$$\frac{dF_{\text{lift}}}{d\varphi} = 0 \longrightarrow \frac{1}{\sqrt{3}} = \cos\varphi_{\max}$$

$$\varphi_{\max 1} \approx 1.216\frac{\pi}{4} \mathrel{\widehat{=}} 54.72^\circ$$

$$\varphi_{\max 2} \approx 2.784\frac{\pi}{4}$$

The total exposed surface is the determining factor for this. More particles impact the plate at larger angles and contribute to the lift force. The numerical simulation gives proof for that, well recognizable in Fig. (4.10).

The drag force has its peak at $\frac{\pi}{2}$, comprehensibly where a gets a particle broadside. It goes down to a minima at zero after a quarter of a period when the trickle b is exposed. The drag force minima cf. Fig. (4.7) and (4.9) have shifted to this bottoms.

$$\tan\varphi = \frac{b}{a} = 0 \Longleftrightarrow \varphi = 0 \qquad \tan\left(\varphi - \frac{\pi}{2}\right) = \frac{a}{b} \approx \infty \Longleftrightarrow \varphi = \pi$$

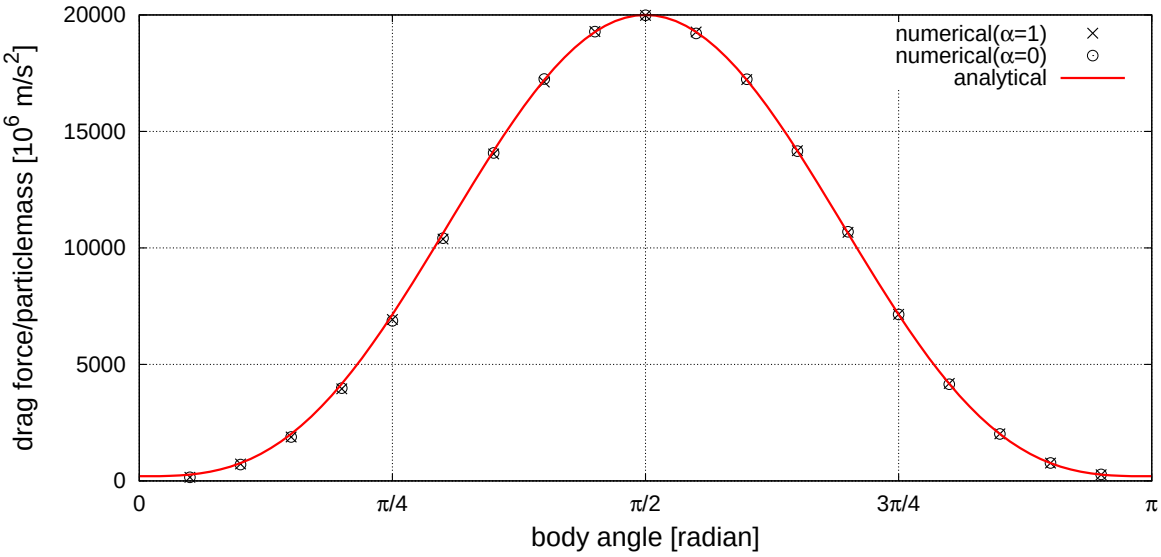

Figure 4.11: Drag force of a flat plate as a function of rotation angle, $a = 0.1\text{m}$, $b = 0.001\text{m}$, $v = 100\text{ms}^{-1}$, $\omega = 5\pi/100\text{s}^{-1}$, $n_0 = 10^7\text{m}^{-2}$.

4.3 Regular n-sided polygon

In chapter 3.1.3 it was shown that the Magnus force has a linear dependence on the current body angle, in case it consists of an odd number of polygons. If the number is even, the Magnus force is steady. Numerically the triangle and the hexagon are studied.

4.3.1 Triangle

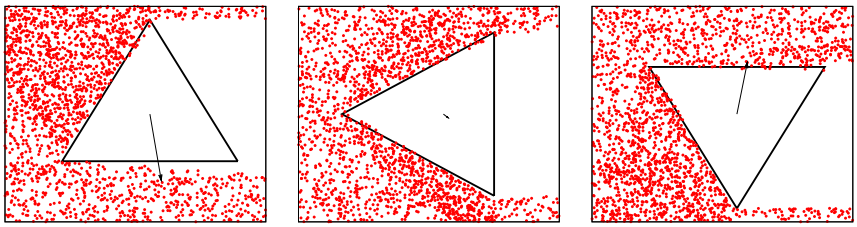

The Magnus force for a triangle unfolds from Eqs. (3.19) and (3.20) to:

2 exposed sides:

$$F_{\mathrm{Mag}} = mn_0\alpha\omega v\frac{a^2}{8}\frac{1}{\sqrt{3}}\left[3 + 2\sin^2\varphi - \sqrt{3}\sin 2\varphi\right]$$

1 exposed side:

$$F_{\mathrm{Mag}} = mn_0\alpha\omega v\frac{a^2}{8}\frac{1}{\sqrt{3}}\left[3 - \frac{\sin 3\varphi}{\sin\varphi}\right]$$

To yield the Magnus force and no other lift force, it is essential to run simulations for $\alpha = 0$ as well as $\alpha = 1$ and finally calculate the difference by subtracting the numbers. This method has therefore a large error which can be minimized by phase-averaged simulation and high particle densities. For 100 phases the following angle functionality got computed:

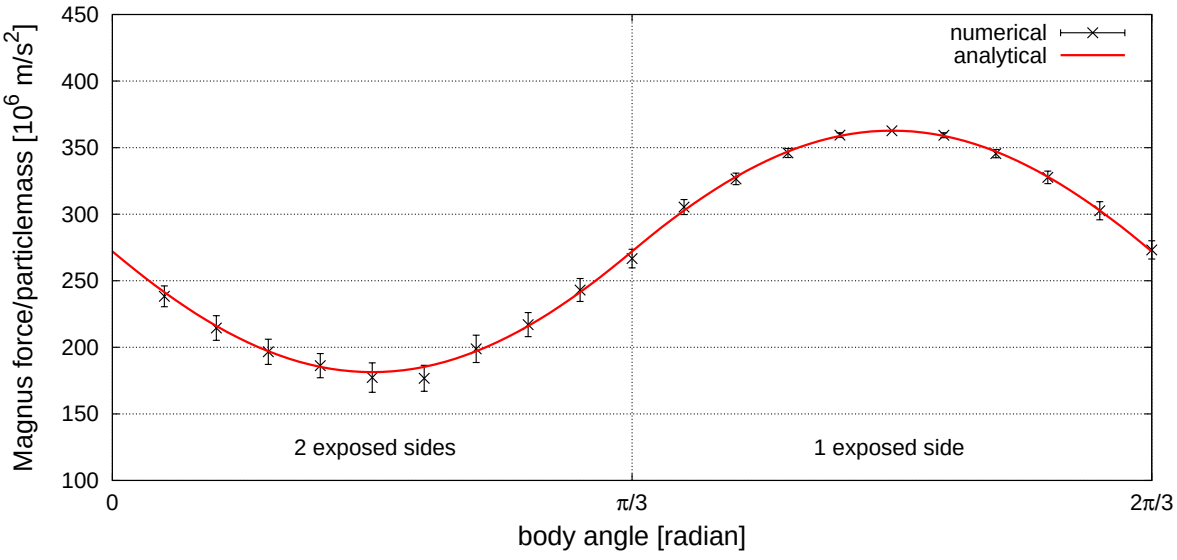

Figure 4.12: Magnus force of a triangle as a function of rotation angle, phase-averaged over 100 phases with double standard deviation, $a = 0.1\mathrm{m}$, $v = 120\mathrm{ms}^{-1}$, $\omega = 2\pi/60\mathrm{s}^{-1}$, $n_0 = 10^7\mathrm{m}^{-2}$.

The Magnus force reaches a minimum exposing two sides to the flow at:

$$\frac{dF_{\mathrm{Mag,2sides}}}{d\varphi} = 0 \Longrightarrow \tan 2\varphi_{\min} = \sqrt{3}$$

$$\Longleftrightarrow \varphi_{\min} = \frac{\pi}{6}$$

Here, incoming flow vector and tangential momentum vector of the triangle stay in a plain angle so that only small momenta in y-direction contribute. Approximately, a Magnus force value twice as much is reached if one side is exposed, the angle is in fact perpendicular, with its peak at:

$$\frac{dF_{\mathrm{Mag,1side}}}{d\varphi} = 0 \Longrightarrow 3\tan\varphi_{\max} = \tan 3\varphi_{\max}$$

$$\Longleftrightarrow \varphi_{\max} = \frac{\pi}{2}$$

Examining Fig. (4.12) one observes that the single exposed side has smaller error bars than the two exposed sides. This can be traced back to particle density irregularities. The two sides are more vulnerable to fluctuations because missing or excess particles leading to errors for both sides at worst summing each other.

In the case of a single exposed side you can see that the error is dependent on the total number of particles hitting the surface. Therefore, the error is minimal if the whole side is exposed to the flow and here the maximum number of particle intersects the surface. At the separation point in case two sides are exposed the error is larger, because the effective length is reduced according to $a\cos(\pi/6) \approx 0.87a$. It is worth noting that the numerical solution agrees within the statistical error bars with the analytical one.

4.3.2 Hexagon

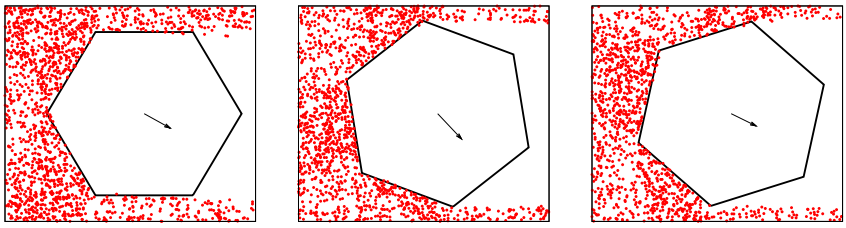

From Eq. (3.18) one expects the Magnus force to remain constant for each angle:

$$F_{\mathrm{Mag}} = mn_0\alpha\omega v\frac{3a^2}{8}\cot\left(\frac{\pi}{6}\right)$$

With $a = 0.1\mathrm{m}$, $v = 120\mathrm{ms}^{-1}$, $\omega = \pi/60\mathrm{s}^{-1}$, $n_0 = 10^7\mathrm{m}^{-2}$ and $\alpha = 1$ this yields:

$$\frac{F_{\mathrm{Mag}}}{m} = 408,1 \cdot 10^6\frac{\mathrm{m}}{\mathrm{s}}$$

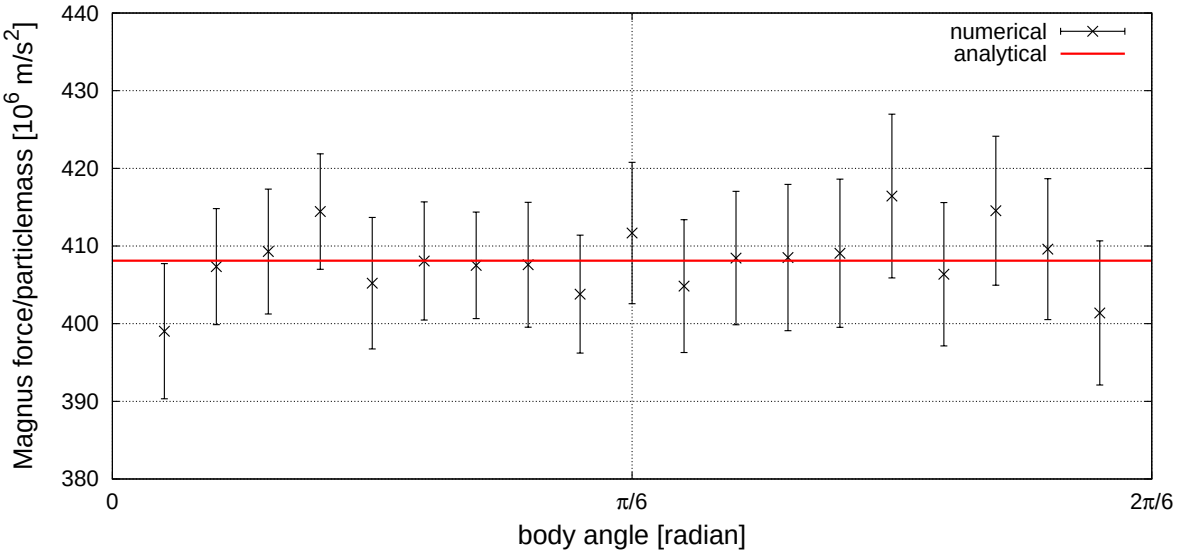

Figure 4.13: Magnus force of a hexagon as a function of rotation angle, phase-averaged over 100 phases with double standard deviation, $a = 0.1\text{m}$, $v = 120\text{ms}^{-1}$, $\omega = \pi/60\text{s}^{-1}$, $n_0 = 10^7\text{m}^{-2}$.

For the same reasons as for the triangle the more sides are exposed the larger is the error because less particles strike a single side and individual errors of all polygons accumulate. With an overall error of about 2% the hexagon computation is quite exact nonetheless so that the steadiness could be validated.
Analysis with more polygons would require extremely high densities as well as high time resolution to distinguish small angles.

Chapter 5

Conclusion and outlook

The aim of the present work was to develop and validate the particle model of a rarefied gas stream by analytical solutions. A rarefied gas flow consists of free particles with respectively high free mean paths compared to the dimensions of the body inside the stream so that no particle to particle impacts take place. This strong simplification ensures reasonable computing times for numerical approaches and a simplified analytical treatment without the need for considering the full Navier-Stokes fluid equations. In the regime of rarefied gas flow the Magnus force is acting in opposite direction as in the continuous flow regime.
Particle simulations were done for simple geometries of rotating bodies like cylinders, rectangles as well as for hexagons and triangles allowing a direct comparison with the analytical model. The flow was modeled by independent particles following straight stream lines intersecting the rotating bodies. For sufficiently good statistics the particle simulations agreed with the analytical model.
In the case of a rotating cylinder error propagation was analysed assuming a Poisson distribution of the errors for the number of particles hitting a body surface fraction during a time period. Drag and lift force obey the same Gaussian distribution function. The errors for the lift force were one order of magnitude smaller than for the drag force which resulted in higher fluctuations for the lift force.
For arbitrary rectangular bodies the total acting force on the body is lowest if the drag force reaches a minimum. Reducing one side of the rectangle the Magnus force scales proportional to the mass of particles displaced by the body. This is also a general result for any rotating object. The Magnus force gets only steady state in case of an even n for regular n-sided polygons.
The successful validation of the numerical model demonstrates that the simulations can be extended to more complicated objects like crescent or ellipse. More complex extensions require a particle to particle collision model. The simplest model could be the Variable Hard Sphere (VHS) model where particle collisions are treated elastically. A more detailed description of particle interactions including internal energy exchange, chemical reaction and thermal radiation is the computationally expensive Larsen-Borgnakke model. However, all this extensions require large scale parallel computing far beyond the scope of this work.

Bibliography

[1] I. Newton. *A new theory about light and colors*. Philos. Trans. R. Soc. London, 1672.

[2] N. Liu and D.B. Bogy. Forces on a rotating particle in a shear flow of a highly rarefied gas. *PHYSICS OF FLUIDS*, 20:1 – 5, 2008.

[3] P. Weidman and A. Herczynski. On the inverse magnus effect in free molecular flow. 16:L9 – L12, 2003.

[4] L.W. Alaways. *Aerodynamics of the Curve-Ball: An Investigation of the Effects of Angular Velocity on Baseball Trajectories*. PhD thesis, University of California, Davis, 1998.

[5] A. Abdallah. Fundamental aspects of rarefied gas dynamics and hypersonic flow. 16:1 – 8, 2004.

[6] F. Coron, J.K. Harvey, and Lengard J.C. Rarefied gas flow simulation: a review. *SAO/NASA Astrophysics Data System (ADS)*, pages 67 – 72, 1994.

[7] A.N. Volkov. Aerodynamic coefficients of a spinning sphere in a rarefied-gas flow. *Fluid Dynamics*, 44:141 – 157, 2007.

[8] I. Newton. *Mathematical Principles of Natural Philosophy*, volume 2 of *translated by A.Motte and F. Cajori (1952)*. Encoclopedia Britannica, Chicago, 1687.

[9] K.I. Borg, L.H. Soederholm, and H. Essen. Force on a spinning sphere moving in a rarefied gas. *Physics of Fluids*, 15:736 – 741, 2003.

[10] I.S. Gradshtey and I.M. Ryzhik. *Table of Integrals, Series and Products*, volume 5.th edition. edited by A. Jeffrey, 1994.

Acknowledgements

Writing a scientific thesis, and in particular if it is the first time, is connected with tiring periods of gathering information and suffering setbacks. At the end of this work I would like to express my gratitude to all people who helped and supported me to overcome this burdens. First of all my thanks are due to my supervisor Prof. Dr. Ralf Schneider for all his good advices and his unrestricted availableness in case of questions. Secondly, I would like to thank my group members for kindly sharing the office with me and giving mental as well as technical help. Finally, I want give thanks to my family and in particular to my grandfather for his continuous scientific inspiration.